Available online at www.sciencedirect.com
ScienceDirect
Journal of Magnetic Resonance 191 (2008) 78–92
JMR Journal of Magnetic Resonance
www.elsevier.com/locate/jmr

Resonator with reduced sample heating and increased homogeneity for solid-state NMR

Alexander Krahn [a,b], Uwe Priller [a], Lyndon Emsley [b], Frank Engelke [a,*]

[a] Bruker Biospin GmbH, Silberstreifen, D-76287 Rheinstetten, Germany
[b] Laboratoire de Chimie, UMR 5182 CNRS/ENS-Lyon, Ecole Normale Supérieure de Lyon, 46 Allée d'Italie, 69364 Lyon, France

Received 23 August 2007; revised 29 November 2007
Available online 9 January 2008

Abstract

In the application of solid-state NMR to many systems, the presence of radiofrequency (rf) electric fields inside classical solenoidal coils causes heating of lossy samples. In particular, this is critical for proteins in ionic buffers. Rf sample heating increases proportional to frequency which may result in the need to reduce the rf pulse power to prevent partial or total sample deterioration. In the present paper, we propose a multifrequency-tunable NMR resonator where the sample is electrically shielded from the NMR coil by a conductive sheet that increases the magneto-electric ratio. Expressions for the B_1 efficiency as function of magnetic and electric filling factors are derived that allow a direct comparison of different resonators. Rf efficiency, homogeneity, signal-to-noise, and rf sample heating are compared. NMR spectra at 700 MHz on ethylene glycol, glycine, and a model protein were acquired to compare the resonators under realistic experimental conditions.

Keywords: Rf heating of samples; Numerical electromagnetic field simulation; NMR coils

1. Introduction

With the continuous quest for higher sensitivity and spectral resolution, the Larmor frequencies of available NMR magnets are now approaching 1 GHz proton frequency. One side effect of this leads to an increasing challenge in the design of the NMR hardware, in particular in NMR probes, because the geometric and electric dimensions of the resonator, rf components, and rf circuitry, commonly used at lower fields, approach the order of the rf wavelength.

Among the major obstacles we meet the intrinsic imperfections of the NMR resonator itself. For solid-state magic-angle-spinning NMR, where solenoidal coils are widely used, the appearance of high NMR frequencies may lead to a degradation of rf homogeneity and an increase of fringe electric fields in the sample volume that may interact with the bulk electric properties of the sample [1–10,12–16].

Notably biologically relevant solid or "semi-solid" NMR samples, where, e.g., protein molecules are surrounded by water molecules (hydration) to provide stability, are commonly crystallized with significant salt concentrations (on the order of 100 mM), giving rise to ionic conductivity in such samples [7]. In addition dielectric polarization losses may arise from the polarization of the water molecules or the biomacromolecules themselves by the presence of an electric field. An rf electric field E_1 present in such samples will interact with the sample, characterized by a complex-valued effective bulk permittivity ε_r, where this interaction leads to the dissipation of energy by rf heating [1–3,9]. Although applications exist where sample heating during the experiment is intended and appreciated [4,5] it is to be avoided for most biological samples, where it can be catastrophic. Consequently, a reduction of the electric field in the sample volume is necessary to circumvent rf heating and to render the perfor-

* Corresponding author. Fax: +49 721 5161 91129.
E-mail address: frank.engelke@bruker.de (F. Engelke).

1090-7807/$ - see front matter © 2007 Elsevier Inc. All rights reserved.
doi:10.1016/j.jmr.2007.12.004

mance of an NMR resonator independent of the bulk electric sample properties [6,8].

In the case of dilute aqueous solutions, the complex permittivity may be modeled considering the reorientation of the dipolar water molecules by a frequency dependent first order Debye model. For low frequencies, e.g., in the whole NMR frequency range, the losses are dominated by a term containing the sample conductivity σ. For ions in solution, the conductivity is governed by parameters such as concentration, mobility, temperature, hydration number, dissociation, and viscosity. However, for realistic samples with a high degree of hydration, this simple model for the permittivity is not valid anymore [10].

The dielectric permittivity is an intrinsic property of the sample, while the rf field distribution of an empty NMR coil is determined by the geometry and the electric symmetry of the resonator and circuit at the observation frequency. If a sample is placed inside the resonator, the rf fields interact with the sample subject to its dielectric properties resulting in a distortion of the field distribution as compared to the unloaded coil. From first principles it follows that the source of any electric field is either originating from a potential difference (conservative) or from a time-varying magnetic field (non-conservative) and both sources are present inside an arbitrary shaped NMR resonator through (i) a time-varying B_1 field generated by the coil current I and (ii) a potential difference across the coil given by the self inductance L multiplied by the time derivative of the coil current, $\mathrm{d}I/\mathrm{d}t$. For a classical solenoidal coil at NMR frequencies, the conservative term is dominating the rf electric field inside the sample and it is one order of magnitude larger than the contribution of the non-conservative part of the electric field. The resulting rf electric field has a direction along the coil axis [11]. This contribution to the overall electric field increases with the third power of frequency [1] and from this observable fact the problem of sample heating arises.

Some alternative "single-coil" [12–14,17] or "cross-coil" [15,16,18,19] geometries have been proposed that exhibit reduced rf electric fields inside the sample volume. Here single-coil geometry means that the coil exhibits, as for a straightforward solenoidal coil, just two coil ports and that it is compatible with the probe rf circuitry used for solenoidal coils. All these approaches reduce the electric length of the coil and/or seek to concentrate the rf electric field E_1 outside the sample volume. On one hand, reduction of the coil inductance might also reduce the efficiency of the rf magnetic field B_1 of the low frequency channels. On the other hand, by shielding the sample volume from the rf electric field E_1, the B_1 field magnitude might be reduced as well, since some B_1 field is stored outside the sample volume reducing the magnetic filling factor [20].

Taking into account all these considerations, it appears worthwhile to design a resonator or coil that attempts to unite some of the advantages of the solenoidal coil (e.g., rf efficiency) with those of a resonator that exhibits characteristically low E_1 fields in its inner volume. In the present paper, we propose a compact single-coil structure, referred to as *Loop-gap Loaded Coil* (LLC). This resonator combines a classical solenoid with an aligned cylindrical conductive sheet forming a loop-gap cylinder, that effectively shields the sample from the E_1 field while increasing the B_1 homogeneity. Because the entire structure resonates with its own eigenmodes due to the strong magnetic and electric coupling between the loop-gap cylinder and the solenoid, it might be misleading to refer to the conductive shield as a separate and independent (passive) Faraday shield, although the cylinder inside the solenoidal coil leads to a reduction or re-distribution of the rf electric field inside the cylinder. The rf field distribution and the eigenfrequency of such a resonator are determined by the dimensions of the coil, the loop-gap cylinder and the alignment of both.

Because of the compact geometry of the LLC, a high magnetic filling factor can be maintained for both the proton and the low frequency broadband channel of the probe. For reference we will compare electromagnetic field simulations and NMR measurements of a solenoidal coil and our LLC resonator. The parameters compared in this study are B_1 efficiency, homogeneity, rf heating, and the signal-to-noise ratio for ^{1}H and ^{13}C at 700 MHz proton frequency. We show that the LLC in an 3.2 mm MAS system provides a good signal-to-noise ratio, high ^{1}H, ^{13}C, and ^{15}N B_1 fields up to 120, 60, and 50 kHz rf amplitude, respectively, and remarkably reduced sample heating.

2. Theoretical background

We begin with a short discourse on the concept of the *field-to-current efficiency* arising from the reciprocity theorem [20,21,27] which, formulated for NMR conditions, states that resonators or circuits generating a high B_1 field per unit current, B_1^*, at the site of the nucleus will efficiently detect the weak signal induced by the precessing magnetic dipolar moment of that nucleus [22,23]. For an arbitrary shaped coil, the mean B_1 field may be expressed as [24]

$$B_1 = \beta\sqrt{\frac{PQ_\mathrm{L}\eta_\mathrm{m}}{fV_\mathrm{S}}} \tag{1}$$

where β is a factor depending on the resonator or coil geometry, P is equal to the effective rf power supplied to the resonating circuit, Q_L is the quality factor of the resonator, f denotes the Larmor frequency (in Hz), V_S is the sample volume, and η_m stands for the magnetic filling factor defined as

$$\eta_\mathrm{m} = \frac{\int_{V_\mathrm{S}} \mu_\mathrm{r} \mid B_1\mid^2 \mathrm{d}V}{\int_{V_0} \mu_\mathrm{r} \mid B_1\mid^2 \mathrm{d}V} \tag{2}$$

The magnetic filling factor corresponds to the ratio of the magnetic energy stored in the sample volume V_S to the total stored magnetic energy in the entire resonator volume V_0. Note that V_0 includes the entire rf circuitry, e.g., com-

ponents for tuning and matching the probe and stop and trap circuits for isolation of the low-frequency X channel.

We define the *field-to-power conversion efficiency* η_P as the ratio of the nutation field B_1 expressed in frequency units of $f_1 = \gamma B_1/(2\pi)$ to the square root of the probe rf input power necessary to generate this field. Taking into account Eq. (1), η_P can be expressed as

$$\frac{f_1}{\sqrt{P}} = \frac{\beta\gamma}{2\pi}\frac{1}{\sqrt{f \cdot V_S}}\sqrt{\eta_m Q_L} = k_1 \cdot k_2 \cdot k_3 = \eta_P \tag{3}$$

in units of Hz/$\sqrt{\text{W}}$, corresponding up to a factor of proportionality, to the current-normalized B_1 field B_1^*. For the sake of brevity we will refer to η_P in the following to as 'B_1 *efficiency*'. The expression (3) for η_P can be decomposed into the geometry factor k_1, the normalization factor k_2, and the efficiency factor k_3. The quality factor Q_L of the resonator can be further decomposed into the quality factor Q_C encompassing the losses in the rf circuit (e.g., capacitor losses and conduction losses) and the quality factor Q_S representing the bulk loss properties of the sample [24]. It holds

$$\frac{1}{Q_L} = \frac{1}{Q_C} + \frac{1}{Q_S} \tag{4}$$

Thus, if the electromagnetic field distribution of a given coil and the sample Q are known, k_3 can be calculated to be

$$k_3 = \sqrt{\frac{\int_{V_S}\mu_r \mid B_1\mid^2 dV}{\int_{V_0}\mu_r \mid B_1\mid^2 dV}\frac{Q_C Q_S}{Q_C + Q_S}} \tag{5}$$

Note, that by inserting any sample—even an ideal lossless sample with only a real valued permittivity—the rf field distribution is altered. At high frequencies a classical coil might be modeled by an equivalent circuit with parasitic stray capacitances due to the inter-turn capacitance and stray capacitances to the probe shield. Insertion of a sample with a relative dielectric constant larger than unity might change the stray capacitance of the coil and thus changing the resonant frequency and matching condition, which is typically compensated by variable tuning and matching components. However, the influence of the sample on the resonator symmetry and losses is negligible under normal conditions, so that the magnetic filling factor remains unaffected.

Similar to the magnetic filling factor η_m an electric filling factor η_e can be defined as

$$\eta_e = \frac{\int_{V_S}\underline{\varepsilon}_r \mid E_1\mid^2 dV}{\int_{V_0}\underline{\varepsilon}_r \mid E_1\mid^2 dV} = \frac{W^{V_S}_{e,stored} + W^{V_S}_{e,diss}}{W^{V_0}_{e,total}} \tag{6}$$

where the numerator corresponds to the stored and the dissipated electric energy in the sample volume and the denominator is equal to the total stored electric energy in the entire resonator. In the above expression, all losses are represented by the imaginary part of the complex sample permittivity ε_r. Taking into account the sample Q_S and recombining with Eq. (6) the amount of energy dissipated in the sample can be expressed as

$$W^{V_S}_{e,diss} = \frac{\eta_e}{1+Q_S}W^{V_0}_{e,total} = \frac{\eta_e}{1+Q_S}\frac{W^{V_S}_{m,S}}{\eta_m} \tag{7}$$

Thus, for a given B_1 field amplitude and sample (represented by the magnetic energy in the sample $W^{V_S}_{m,S}$ and by the sample quality factor Q_S), the power dissipation in the sample scales with the electric and the inverse of the magnetic filling factor. Note that Q_S represents the sample loss properties, while η_e and η_m are properties of the NMR probe. The ratio of the magnetic and the electric filling factor is usually referred to as the magneto-electric ratio η_{me}, as proposed, e.g., by Doty [24].

However, both filling factors are linked together by the coil geometry and depend on the frequency at which the resonator is operated. Therefore, any attempt to reduce η_e will also have an impact on η_m. Consequently, any coil design that is intended to reduce rf sample heating seeks to minimize η_e while keeping an acceptable η_m at all frequencies (channels) of interest. In the following chapter we will present a structure that fulfills this criterion by effectively reducing the E_1 field inside the sample volume, while minimizing the degradation of the B_1 field.

3. The LLC resonator

3.1. General considerations

The major contribution to the rf electric field E_1 in the sample volume of a 'classical NMR solenoidal coil' originates from the potential difference caused by the time derivative of the coil current multiplied by the coil inductance L [11,16]. For a symmetrically driven coil, the potential is maximum at either coil end with opposite sign giving rise to an conservative electric field inside the sample volume. At the coil ends, the boundary conditions at the conductive surface of the coil wire enforces a radial electric field component, whereas close to the coil center the dominating electric field component is axial. Additionally, a local electric field maximum occurs at the coil center due to the potential difference between all turns. The E_1 field can be reduced by inserting an insulated conductive cylindrical sheet with a longitudinal gap concentric with the solenoid according to Fig. 1a. In the radial space between coil wire and this loop-gap cylinder, the E_1 field has only a radial component, since for the symmetrically driven coil the potential of the cylinder is at virtual ground.

Perfect conducting surfaces require the electric field to be normal while the magnetic field has only a tangential component inducing a current on the surface [21,27]

$$\begin{aligned}\vec{n}\times\vec{E}_1 &= 0\\ \vec{n}\times\vec{B}_1 &= \vec{J}\end{aligned} \tag{8}$$

where $\vec{n}$ denotes the unit vector normal to the surface element. The disturbance of the B_1 field due to the presence

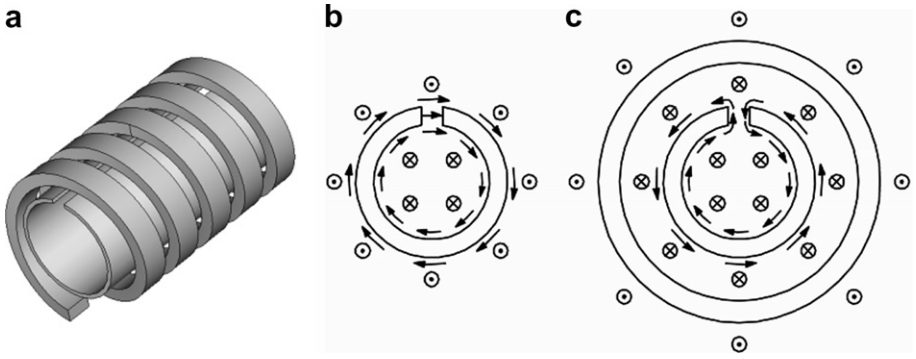

Fig. 1. (a) Geometry of the LLC resonator: inside the solenoid a conductive loop-gap (LG) cylinder shields the sample from the electrical field generated by the coil. Solenoid and cylinder are insulated from each other by a dielectric tube (not shown). (b) Principal distribution of the B_1 field and surface currents for the classical LG mode in a transverse plane. The direction of the surface currents on the outer and inner surface are the same and continue as a displacement current across the gap. For the DLG mode (c), the surface currents induced by the solenoidal coil on the outer surface return in opposite directions on the inner surface of the loop-gap cylinder. Due to the short electrical length of the cylinder in azimuthal direction, the displacement current across the gap is negligibly small.

of the loop-gap cylinder can be considered in a similar manner. The B_1 field generated by the coil induces an azimuthal surface current $I_{\varphi 0}$ on the outer surface of the loop-gap cylinder. Likewise the z component of a magnetic field inside the cylinder will impose a surface current $I_{\varphi I}$ on the inner surface. With respect to the direction of these azimuthal surface currents two principal modes can be distinguished, namely (i) the classical *loop-gap* mode (*LG* mode) [25,26] as an eigenmode of the loop-gap cylinder, and (ii) a *driven loop-gap* mode (*DLG* mode) [28] as an eigenmode of the joint system loop-gap cylinder plus solenoid.

For a distinction of these modes, only the current distribution on the inner and outer surface of the loop-gap cylinder and the field and current distribution in the close vicinity of the longitudinal gap need to be considered. In the case of the classical LG mode, an azimuthal surface current $I_{\varphi 0}$ flowing on the outer surface can continue as a displacement current across the gap (Fig. 1b). Consequently, on the inner surface a current $I_{\varphi I}$ with the same direction is present resulting in a B_1 field pointing in opposite direction inside and outside the loop-gap cylinder as is indicated by the circles corresponding to magnetic flux lines with a direction orthogonal to the drawing plane.

The frequency of the LG mode is determined, up to the first order by the inductance of the loop-gap cylinder representing a single-turn coil with a stray capacitance across the gap. Thus the LG mode is an eigenmode of the loop-gap cylinder. On the other hand, a DLG mode can be excited in which the surface current $I_{\varphi 0}$ is induced by the magnetic field of a coil wrapped around the insulated cylinder (Fig. 1c). Since for the geometry under discussion here and for NMR frequencies the circumferential length of the cylinder is short compared to the wavelength (i.e., $\lambda_0 \gg D\pi$, where D is the cylinder diameter) the displacement current across the gap is negligible and the current $I_{\varphi 0}$ is enforced to flow through the gap to the inside of the cylinder and returns in opposite direction on the inner surface as current $I_{\varphi I}$. This is possible because the radial penetration depth (skin depth δ, [21,27,28]) of the current is much thinner than the thickness of the cylinder. Throughout the NMR frequency range and for typical conductors $\delta \sim 2\ldots10$ μm, while realistic radial thickness dimensions for a cylinder are on the order of 100 μm. Due to the direction of the currents, the direction of the B_1 field close to the cylinder surface must be the same inside and outside the cylinder as illustrated schematically in Fig. 1c.

The application of a similar structure, employing the classical LG mode for proton frequency and the DLG mode for X frequencies has been proposed by Cory and coworkers [28]. Because of the aforementioned short electrical length of the cylinder, additional tuning capacitors across the gap would be necessary to tune the eigenresonance of the loop-gap cylinder to the proton frequency (see, e.g., [18,19]). A similar system of two overcoupled resonators where a tuned microcoil circuit was placed inside an outer solenoid was successfully applied by Sakellariou et al. [29] with the goal of increasing sample filling factors (hence sensitivity) for small-volume (nanoliter) samples and achieving high rf magnetic field amplitudes. In contrast to [28], here we propose to use the DLG mode for the proton frequency as well. The advantage of this approach is twofold. On one hand, the loop-gap cylinder represents a mutual inductance for the primary solenoidal coil, compensating for the necessary increase of the coil inner diameter as compared to a tightly wound solenoid. As a consequence in a given probe circuit the coil can be exchanged with an LLC without major changes to the probe circuit electronics. On the other hand, the surface currents redistribute on the cylinder surfaces. We obtained by simulation (details see next section) the principal current density distribution (Fig. 2) on the outer and inner surfaces of the loop-gap cylinder surrounded by a solenoidal coil (Fig. 1a). The currents induced on the outer surface pass through the gap, resulting in a current re-distribution inside the cylinder where close to the axial edges the current density is higher than the current at the

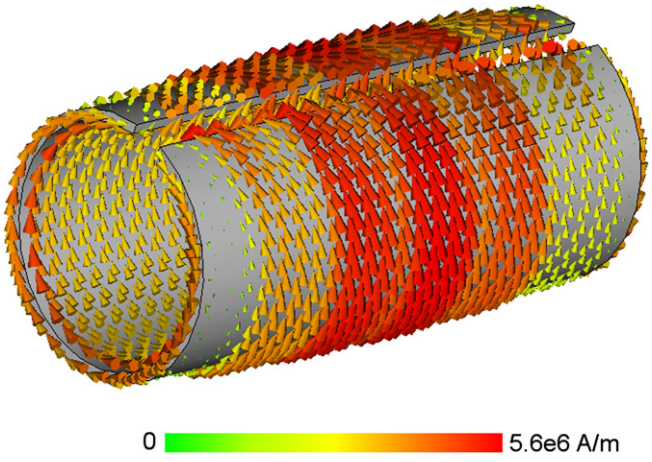

Fig. 2. Simulated surface current distribution on a loop-gap cylinder induced by the magnetic field of an (insulated) solenoidal coil wound around that cylinder. If the clearance between the coil wire and the surface of the cylinder is small, the magnetic field in this region is large leading to an increased surface current in the outer surface of the cylinder. Due to the short electrical length of the loop-gap cylinder in azimuthal direction, the electric field across the gap, and therefore the displacement current across the gap, is negligibly small and the surface current passes through the longitudinal gap to the inside of the cylinder and returning in opposite direction. When passing through the longitudinal gap, the surface current inside the cylinder redistributes with a maximum current density at the axial ends giving rise to a homogenized B_1 distribution.

center, [30] leading to an increased B_1 homogeneity for the sample volume. It is because of the inductive loading of the primary coil by the mutual inductance of the loop-gap cylinder that we named our structure the "loop-gap loaded coil" or LLC resonator.

Naturally, the straightforward application of boundary conditions as discussed above only predicts the fields in close vicinity to the boundaries imposed by the conductive cylinder. A more detailed rf field solution requires a rigorous method to solve Maxwell's equations in the entire resonator volume.

3.2. Numerical electromagnetic field simulations at 700 and 176 MHz

To obtain a detailed field distribution for a given structure, the coupled system of Maxwell's equations has to be solved according to the boundary conditions imposed by the geometry. However, analytical solutions are only possible for structures that provide a high degree of symmetry, which is normally not the case for realistic geometries. Due to the computational power available today, numerical methods are available that allow the solution of three dimensional electromagnetic fields inside arbitrary shaped materials and for arbitrary boundaries. All field calculations to be shown in subsequent sections have been performed with commercially available software (CST Microwave Studio (MWS), Darmstadt, [32]) employing a discrete formulation of Maxwell's equations on a hexagonal grid [31].

In the following we have solved for the field distribution at 700, 176, and 71 MHz (corresponding to the ^{1}H, ^{13}C, and ^{15}N Larmor frequencies in a static magnetic field of 16.4 T) for the two structures to be compared, namely (i) a classical solenoidal coil (inner diameter ID = 3.4 mm, length $L = 8$ mm, 5 turns of flat wire with cross section 0.9 mm × 0.45 mm) and (ii) our LLC (with ID = 3.4 mm, wall thickness of 0.15 mm, and gap width of 0.5 mm). The inner dimensions of the resonators were chosen with some extra radial clearance to house an MAS sample rotor with 3.2 mm outer diameter.

We have employed the MWS eigenmode solver, based on the Jacobi–Davidson method [32], that is particularly useful to compute eigenfrequencies and corresponding field patterns for geometries without open boundaries. With this method no coupling structure needs to be modeled and therefore, no unwanted effects originating from the coupling structure need to be considered.

The simulation model of the solenoid was constructed with the dimensions given above, with short leads at either coil end, each terminated by a 2 mm × 2 mm plate which form two capacitors with the boundary of the computational domain. This boundary was set up to be perfectly electric conductive (PEC), i.e., it holds $\mathbf{E} \times \mathbf{n} = 0$: the tangential electric field vanishes at the boundary surface. The boundary capacitors were filled with a dielectric material of variable permittivity ε_r to tune the solenoid to the respective NMR frequency of 700, 176, and 71 MHz. In order to mimic a realistic situation, we have modeled an MAS rotor of 3.2 mm outer diameter, 2.1 mm inner diameter, and length 12.4 mm resulting in a sample volume of 42 μl, where the rotor material was assigned with a (real valued) relative permittivity of $\varepsilon_r = 32$ corresponding to the permittivity of ZrO_2 ceramics. As sample volume an empty cylinder volume ($\varepsilon_r = 1$) of length 5 mm was considered, that was placed inside the rotor and centered with respect to the resonator (Fig. 3).

The magnetic and electric field distributions of the classical solenoidal coil are well understood and have been discussed by various authors (see, e.g., [11,33–35]). We show it here (Fig. 4a and b) for comparison with the distribution obtained for the LLC (Fig. 4c–f). While in our numerical model most of the overall electric energy is stored in the capacitors, some electric field is present around the center of the solenoidal coil (Fig. 4a) and it is this part that is responsible for sample heating. A profile of the electric field along the solenoidal-coil axis is plotted in Fig. 5a. The situation changes significantly when the loop-gap cylinder is inserted in the solenoid (Fig. 4c). To provide the same sample volume, the LLC model consists of a slotted cylinder with an inner diameter of 3.4 mm, thickness of 0.15 mm, and a gap width of 0.5 mm. To insulate the cylinder from the solenoidal coil, a PTFE tube ($\varepsilon_r \sim 2.1$) with an inner diameter of 3.7 mm and a thickness of 0.25 mm was modeled around the cylinder. Thus for the 5-turn driving coil an inner diameter of 4.2 mm results whereas the coil length remained the same as for the solenoid.

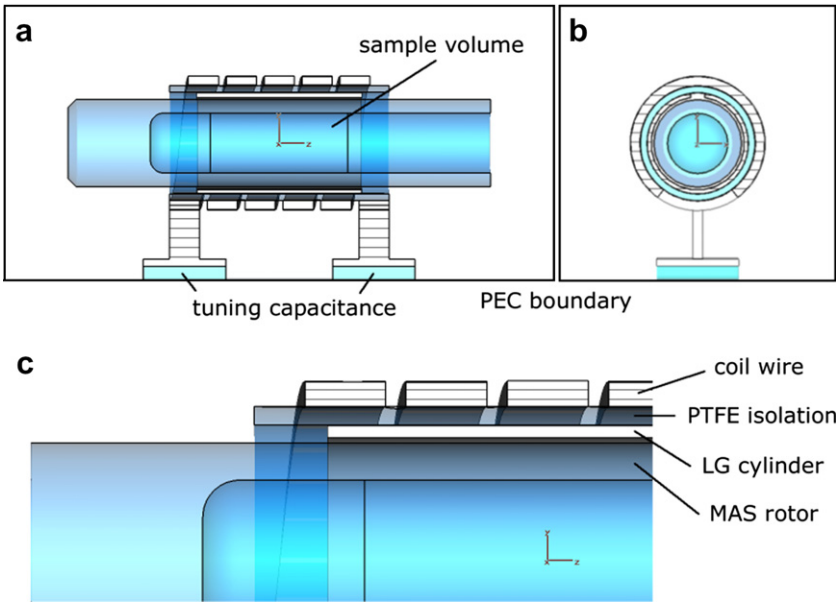

Fig. 3. Model setup for the numerical simulation to obtain the field distribution of the LLC resonators (a) in the axial y–z plane and (b) the transversal x–y plane. An expanded view (c) of the longitudinal cross section illustrates the different radial layers of the LLC, the outer solenoid, the teflon tube, and the loop-gap cylinder. An MAS rotor with the dielectric properties of ZrO_2 was modeled inside the LLC. The resonator is tuned to a given resonance frequency by two plates at either end of the coil leads that form a capacitor with the perfectly electrically conducting boundary of the computational domain. The frequency is adjusted by filling the gap between plate and boundary with a dielectric material of variable permittivity. The field distribution of such a setup can be calculated by solving for the eigenmodes of the resonator without taking into consideration a coupling structure.

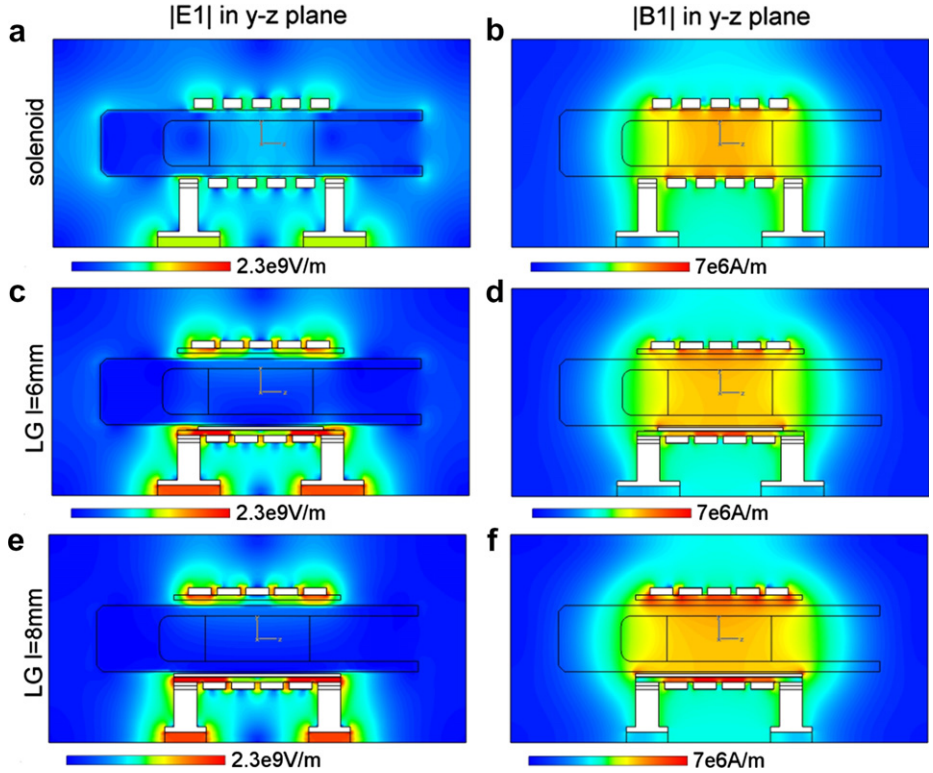

Fig. 4. Simulated electromagnetic field distribution for the geometries under consideration at 700 MHz. The rows illustrate the three structures discussed in the text, the solenoidal coil (a and b), the LLC with an aligned loop-gap cylinder of length 6 mm (c and d) and an LLC with a longer cylinder of length 8 mm (e and f). The columns show the electric (a, c, and e) and magnetic field magnitudes (b, d, and f) on a logarithmic scale in an axial plane of the coil. Inside the resonators an MAS rotor of permittivity $\varepsilon_r = 32$ is considered together with a restricted sample of 2.2 mm diameter and 5 mm length with vacuum permittivity that was used to calculate the filling factors.

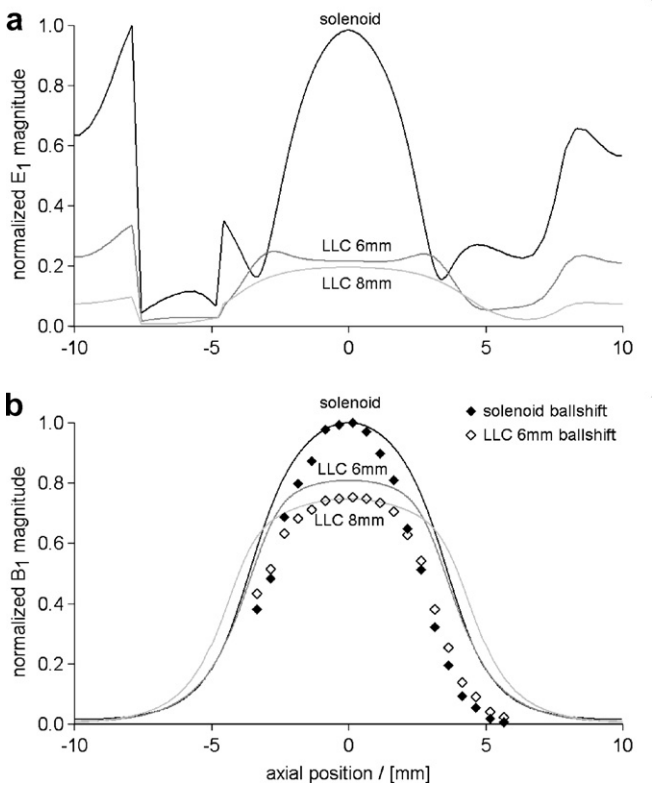

Fig. 5. (a) Simulated electric field profiles along axes of the solenoid and of the LLC (of 6 mm or 8 mm cylinder length). For the solenoid, a local maximum around the coil center occurs where the sample is located, while the peak electric field value is significantly reduced for the LLCs. The discontinuities at the left hand side are due to the bottom of the high-ε_r MAS rotor that was considered in the simulation model. (b) In the same way, the magnetic field profiles for the solenoid and the LLC were calculated (solid curves). For the LLC an increased homogeneous region around the center is observed, due to the distributed wall currents on the inner cylinder surface. Experimental data from ballshift measurements are indicated by symbols.

The peak electric field occurs in the space between the outer turns and the loop-gap cylinder since for the symmetrically driven solenoid the cylinder is a virtual ground (Fig. 4c) as discussed above. Therefore, the clearance between solenoid and cylinder has to be chosen carefully to be small enough to obtain a good magnetic filling factor. On the other hand, the clearance has to remain large enough to prevent high voltage breakthrough. For the symmetrically driven LLC, the peak magnetic field appears in the space between the center turn and cylinder, driving the surface current in the cylinder. The surface currents inside the cylinder are distributed in such a way that they give rise to an increased B_1 homogeneity inside the sample volume (Figs. 2 and 4d).

The field profiles for electric and magnetic fields along the coil axis for the solenoid and the LLC are given in Fig. 5 normalized relative to the respective maxima for the solenoidal E_1 and B_1 fields. Comparison of the E_1 field profiles indicates a reduction of the peak electric field by 75% for the LLC as compared to the peak value for the solenoid. On the other hand the magnetic field profile shows a substantially increased homogeneous region around the center region while the peak B_1 field is decreased by 20%.

If the axial length of the loop-gap cylinder is increased, the electric stray field of the driving coil is almost completely confined between coil and cylinder peaking at the outer turns (Fig. 4e). The B_1 field again exhibits a homogenized profile whose shape is mainly determined by the current distribution inside the loop-gap cylinder (Fig. 4f), thus leading to an increased homogeneous region. Consequently, the parasitic coil capacitance is increased that results in a reduction of the eigenfrequency of the LLC. The dependence of the eigenfrequency and the magneto-electric ratio on the axial length of the loop-gap cylinder for the aforementioned model geometry is plotted in Fig. 6.

From the field distribution, the filling factors according to Eqs. (2) and (6) can be calculated for a model sample volume of 2.2 mm outer diameter and 5 mm centered at the resonator axis. The calculated filling factors are given in Table 1. While the calculated magnetic filling factors are reduced by approximately 30% for the LLC as compared to the solenoid, the electric filling factor is reduced by an order of magnitude.

From the field distribution we also calculated the Q factors for both resonators taking into account a lossless ($\varepsilon'' = 0$) rotor made from high permittivity material ($\varepsilon' = 32$). Since the dielectric properties of the rotor and the teflon tube were considered to be lossless, the only contribution to the losses in the simulation is due to an assumed finite conductivity of 58×10^6 S/m for the materials of the solenoid, the loop-gap cylinder and the boundary of the computational domain.

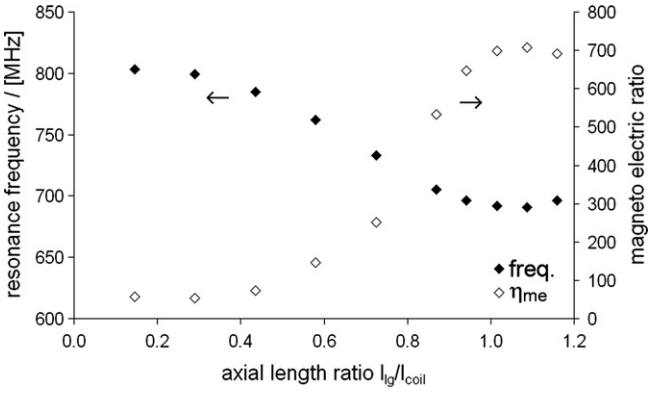

Fig. 6. Resonance frequency and magneto-electric ratio as function of the axial length of the loop-gap cylinder for a sample volume of outer diameter 2.2 mm and an axial length of 5 mm. The data were calculated with a model that yielded the field distributions according to Fig. 3c and d with the axial length of the loop-gap cylinder varied from 1 to 8 mm. For a short cylinder and a balanced coil, the potential difference between the center turn of the solenoid and the cylinder is negligibly small. As the axial length increases, the eigenresonance frequency decreases due to the capacitance formed by the outer turns of the solenoid with the cylinder. The magneto-electric ratio η_{me} increases as the loop-gap cylinder shields the electric field originating from the potential difference between the coil turns.

Table 1
Comparison of the calculated magnetic and electric filling factors, η_m and η_e, resonator Q values as well as the magneto-electric ratio η_{me} of the model system

Resonator	Simulation data						
	V_C [mm^3]	η_m [%]	η_e [%]	η_{me} []	Q_0 []	Q_{load} []	$l_{90\%}$ [mm]
700 MHz							
Solenoid	73.8	20.4	0.258/3.6	79	594	118	3.58
LLC	72.6	13.9	0.024	579	298	281	4.79
176 MHz							
Solenoid	73.8	20.4	0.025	812	292	184	3.86
LLC	72.6	13.2	0.0012	11000	159	153	5.03
71 MHz							
Solenoid	73.8	17.6	0.004	4400	192	159	3.96
LLC	72.6	12.6	0.00032	39375	99	99	5.03

As sample volume, an empty cylinder with an outer diameter of 2.2 mm and length of 5 mm was considered. Q_0 denotes the Q factor of the resonator with empty rotor (i.e., sample volume empty). Q_{load} is equal to the Q factor if the sample volume is filled with a sample with relative permittivity of $\varepsilon_r = 76$ and conductivity $\sigma = 0.5$ S/m. Additionally, we tabulated $l_{90\%}$ as the length along the resonator axis, within which the B_1 field magnitude is >90%. V_C denotes the resonator volume.

As expected, the quality factor of the LLC is reduced to half of the value calculated for the solenoidal coil. Contributions arise from the surface currents in the loop-gap cylinder and from wall currents in the bounding box of the calculation domain, but the latter are an order of magnitude smaller, thus the Q value is dominated by the resonator losses. However, we repeated the calculation considering a lossy saline sample of 45 mM salinity corresponding to a relative permittivity of $\varepsilon_r = 76$ and a conductivity of $\sigma = 0.5$ S/m at a frequency of 700 MHz. At this frequency the effect of the lossy sample on the Q value of the solenoidal coil is dramatic. A reduction by 80% was calculated. In contrast, the LLC's Q value remained almost unaffected (Table 1).

Finally, we calculated the length $l_{90\%}$ on the resonator axis, along which the B_1 field magnitude is within 90% of the field magnitude at the resonator center. We find a 90% homogeneous region of 3.6, 3.9, and 4 mm for the solenoidal coil and 4.8, and 5 mm for the LLC at ^{1}H, ^{13}C, and ^{15}N frequencies (Table 1), respectively.

4. Experimental results

4.1. Fabrication of the LLC

Due to the small dimensions of the LLC every part had to be produced with a high degree of accuracy. The outer coil of the LLC was made of susceptibility compensated wire [36,37] with a rectangular cross section of 1.1 mm × 0.35 mm. The wire was wound on a center core of 3.9 mm outer diameter. When the force is removed after the winding procedure, the coil diameter increased to 4.3 mm. In order to insulate the coil from the inner cylinder, we used a tube consisting of native PTFE. The inner diameter of the insulating cylinder was achieved by drilling a hole of 3.8 mm diameter into a solid PTFE cylinder. A metallic core of similar outer diameter was inserted into the cylinder to provide mechanical stability for further machining. The outer diameter was adjusted on the lathe to the desired value of 4.3 mm with a small feed rate to achieve a smooth surface.

As for the coil wire, we used a flat sheet of susceptibility compensated metal that was wrapped around a core to form the loop-gap cylinder. To avoid arcing problems, special care was taken during the assembly of the LLC, such that no radial gaps occurred between the cylindrical interface layers, i.e., between coil wire and PTFE tube, and between PTFE tube and loop-gap cylinder.

The self resonance of the solenoid with leads mounted on a boron nitrate coil holder was measured with a pick-up coil to be 1153 ± 2 MHz which decreased after the insertion of the teflon tube and the loop-gap sheet to 870 ± 1 MHz due to the capacitance formed by the coil wire and the sheet.

4.2. Rf bench tests and NMR pulse calibration

For a direct comparison of two NMR resonators, both have to be operated in the same rf circuit environment. We used a 700 MHz ^{1}H/^{15}N–^{13}C double resonance probe with

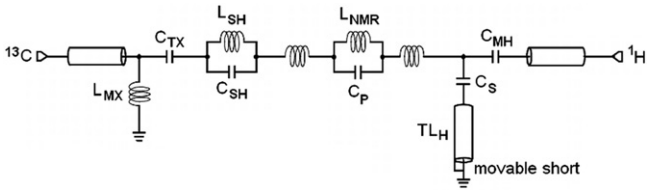

Fig. 7. NMR probe circuit as applied in this comparative study. It provides a broad tuning range, hence it was possible to tune and match both resonators without any changes to the circuit topology or the values of the fixed elements. The resonator is represented by the sample coil inductance L_{NMR} and the parasitic parallel capacitance C_p connected to the probe circuitry via two lead inductances at either end. To isolate the ^{1}H channel from the X channel and to provide symmetry for the resonator, a ^{1}H stop circuit—inductance L_{SH} in parallel to the capacitance C_{SH}—is used on the X side. ^{1}H tuning and matching is achieved by a shorted transmission line TL_H and the matching capacitor C_{MH}, respectively. Likewise, the X channel is tuned and matched to the feeding line impedance by the tuning capacitor C_{TX} and matching inductance L_{MX}. Additionally, a serial capacitor C_S in series with TL_H provides rf symmetry.

a modified Cross–Hester–Waugh circuit [38] given in Fig. 7 that provides a wide tuning range for both channels. This is necessary to allow an exchange of the two resonators under consideration without changes in the circuitry and to tune and match the solenoid to the lossy samples as discussed in the next section.

In the schematic according to Fig. 7 the sample coil is represented by parallel circuit made of an inductance L_{NMR} and parasitic capacitance C_P connected to the circuit with two lead inductances on either side. To isolate the low-frequency channel (X channel) from the ^{1}H channel and to drive the resonator symmetrically, a proton stop circuit (with capacitance $C_{SH} = 2.2$ pF and inductance $L_{SH} \approx 23$ nH) is connected to the left side of the resonator. Proton tuning is achieved by a short-circuited transmission line (TL_H with shield diameter 8.3 mm, center conductor diameter 5 mm, with air dielectric) of length $L = 90 \pm 10$ mm $< \lambda_{1H}/4$ resulting in an input impedance corresponding to a parallel capacitance at proton frequency. The resonator is matched to the 50 Ω cable by C_{MH}, consisting of a Voltronics trimmer capacitor tunable from 1.0 to 23 pF in series with two 1 pF chip capacitors to reduce the voltage across the trimmer. For X frequencies, the input impedance of the shorted transmission line corresponds to a small inductance in series, thus an extra capacitor C_S needs to be included that provides symmetry for the resonator. The X channel is tuned by a gas filled high voltage capacitor with a tuning range of 1.5–45 pF (Jennings Technology Company, http://www.jenningstech.com) and matched to the 50 Ω cable by a parallel coil with a variable inductance.

Before NMR testing, bench tests were made comparing the loaded circuit Q factors, and B_1 profiles of both resonators. The latter were measured by comparison of the resonant frequency of the resonator with an empty 3.2 mm zirconia MAS rotor ($\varepsilon_r \sim 32$) and the same rotor with a brass sphere of 2 mm outer diameter.

With the definition of the magnetic filling factor in Eq. (2), the perturbation of the magnetic field due to the presence of the brass sphere may be expressed as an apparent change in coil inductance L.

$$\eta_m = \frac{\Delta L}{L} = 1 - \frac{L_p}{L} = 1 - \left(\frac{f_0}{f_p}\right)^2 \tag{9}$$

where $\Delta L = L - L_p$ corresponds to the difference of the unperturbed inductance L and the perturbed inductance L_p, while f_0 and f_p denote the corresponding resonant frequencies with the empty rotor and the rotor together with the metal sphere. Therefore the frequency shift $\Delta f = f_p - f_0$, due to the presence of the metal sphere (in technical jargon commonly referred to as *ballshift*) is proportional to the magnetic energy in the perturbed volume [39].

As a consequence, the B_1 profile can be measured by repeating the measurement with the sphere placed at different axial positions and measuring the frequency shift. With this method, we estimated the B_1 profile of the solenoidal coil and the LLC in the circuit by applying Eq. (9). For comparison, these data were added to the numerical data in Fig. 5. Determined by the ballshift values, according to Eq. (9), the maximum values of the magnetic filling factors $\eta_{m,b}$ at ^{1}H and ^{13}C frequencies are tabulated in Table 2 and confirm the reduction of the peak magnetic field predicted by the simulation. However, the measured B_1 homogeneity, appearing as narrower profiles in Fig. 5 as compared to the profiles obtained by electromagnetic field simulation, has its origin due to two effects: (i) the 2 mm sphere in a 4.3 mm coil or resonator represents a relatively large rf field disturbance (e.g., the volume ratio of the spherical volume to the resonator volume is >5%), hence not only axial, also radial field components affect the ball shift, and the assumption of representing a small perturbation is only approximately valid, (ii) in the presence of electric fields, the sphere increases the inter-turn capacitance of the coil which affects again the field distribution. Nevertheless the measured 90% homogeneous length $l_{90\%}$ (i.e., that length over which the magnetic field amplitude deviation from the maximum value is ⩽10%) of the LLC is 3.9 mm as compared to 2.4 mm with the solenoid for proton frequency.

Table 2
Comparison of the measured bench test data for the solenoid and the LLC resonator

Resonator	Bench test data				
	V_C [mm^3]	$\eta_{m,b}$ [%]	$\Delta f_r/f_0$ [%]	Q at −3 dB []	$l_{90\%}$ [mm]
700 MHz					
Solenoid	73.8	3.93	1.2	190	2.4
LLC	72.6	2.93	0.41	161	3.9
176 MHz					
Solenoid	73.8	4.92	0.13	97	2.4
LLC	72.6	3.75	0.07	72	3.9
71 MHz					
Solenoid	73.8	4.2	0.09	59	2.5
LLC	72.6	3.1	0.07	53	4.1

The ballshift measurements, performed with a metal sphere of outer diameter of 2 mm, centered in a ZrO_2 MAS rotor, yield the magnetic filling factor $\eta_{m,b}$. By using a set of rotors where the axial position of the sphere is systematically varied, we obtain the B_1 profile to derive the 90% homogeneous region $l_{90\%}$. Also shown the relative frequency shift $\Delta f_r/f_0$ originating from the high-permittivity material of the rotor.

In addition in Table 2, we give the relative frequency shift $\Delta f_r/f_0$, with Δf_r being equal to the frequency shift caused by insertion of the (empty) MAS rotor, made of zirconia ceramics of high permittivity ε_r, into the empty resonator. The frequency shift Δf_r due to the presence of the rotor cannot be used to estimate the electric filling factor as defined in Eq. (6), because the rotor interacts mainly with the electric fields at the coil ends and close to the coil wire where normally no sample is present. Nevertheless, for the LLC it indicates already the reduced E_1 field as compared to the solenoidal coil.

The measured circuit Q value of the probe circuit equipped with the LLC is reduced by 15% with respect to the solenoid. This corresponds to the predicted reduction due to the conduction losses of the induced currents in the loop-gap cylinder. Note that the circuit Q factor is affected by all losses in the circuitry, therefore it cannot be compared directly with the Q factors calculated for the numerical models above.

To determine the B_1 efficiency η_P according to Eq. (3), the effective pulse power at the probe input was measured by using an ANRITSU ML2437A power meter. The B_1 field was determined via the NMR π pulse duration with a low-loss reference sample of adamantane, for ^{1}H and ^{13}C, and with a ^{15}N labeled glycine sample for ^{15}N, respectively. The data in Fig. 8 illustrate an approximately linear dependence of the B_1 field on the (square root) power—the efficiency η_P is equal to the slope value of the linear function. The ^{1}H, ^{13}C, and ^{15}N B_1 efficiencies for the adamantane and glycine samples measured with the LLC are reduced by approximately 25% as compared with the solenoidal coil (Table 3). Since η_P depends on the electric filling factor and the sample loss properties, it has to be re-determined when using a lossy sample. Measurements of the B_1 homogeneity using the signal intensity after a 810° pulse as compared to a 90° pulse with a cylindrical sample of outer diameter 2.2 mm and axial length of 5.5 mm length verify experimentally the increased homogeneous region for the LLC. All measurements were made under MAS at 7 kHz spinning rate.

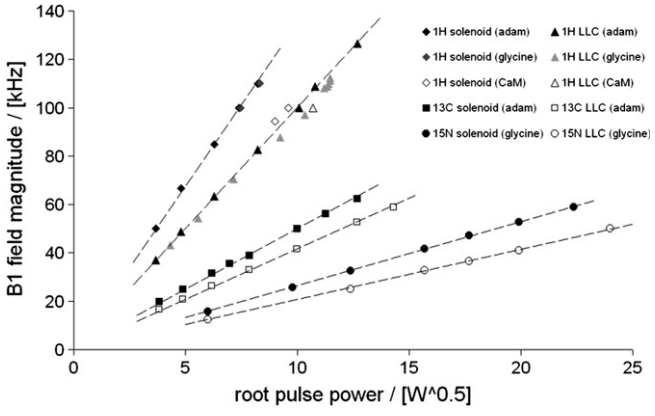

Fig. 8. B_1 efficiencies η_P measured by NMR 90° pulses and rf power levels at the probe input ports corresponding to the slopes of the linear B_1 field as function of the square root pulse power for the ^{1}H, ^{13}C, and ^{15}N channel of the probe equipped with the solenoid and the LLC. Samples were adamantane, glycine and calmodulin (CaM). The maximum effective nutation fields achieved with the LLC were 121, 60, and 50 kHz for ^{1}H, ^{13}C, and ^{15}N. Please note that these numbers do not correspond to any theoretical limit.

4.3. Sample heating

Sample heating can be observed *in situ* if the sample contains nuclear spin species with a calibrated temperature dependent isotropic chemical shift, commonly referred to as NMR thermometer. Traditionally the chemical shift of the hydroxyl protons relative to the ethyl protons in ethylene glycol found widespread application [40–42]. In recent publications also lanthanide compounds [12,43] or bicelles [13] were used to monitor temperature increase due to rf heating in NMR samples.

For biological samples, compounds like tris(trimethylsilyl)methane [44] were shown to be efficient NMR thermometers, since this compound is inert and exhibits a solvent independent linear temperature dependence of the ^{13}C chemical shift between the methine and methyl carbons. However, for most biological samples most conveniently the water peak can be used.

In the following, we took ethylene glycol as an NMR thermometer to (i) characterize the temperature increase due to friction in the bearings of our MAS system, (ii) rf heating during a long decoupling pulse, and (iii) for a study of the temperature evolution in the sample during and after a 100 kHz amplitude rf pulse in the ^{1}H channel. Ethylene glycol exhibits a negligible conductivity—at room temperature we measured a dc conductivity of $\sigma \sim 21 \pm 6$ μS/m. However, ethylene glycol is characterized by a high electric polarization ($\varepsilon_r = 37.7$ at 20 °C) [45]. Therefore rf heating is caused mainly by the work necessary to reorientate the dipoles as the direction of the electric field in the sample volume changes. In our experiments the latter was manifested by the reduction of the circuit Q from 190 to 100 on the proton channel after insertion of a MAS rotor filled with ethylene glycol (42 μl) into our sample coil (solenoid).

Sample heating in solid-state NMR is not only caused by the absorption of rf power, but also by friction in the air bearings of the MAS system. To characterize the latter, we kept the bearing pressure fixed at 1.5 bar while increasing the drive pressure. We observed a temperature increase by 20 K as the spinning speed was increased up to 15 kHz. For spinning speeds below 2.5 kHz the temperature increase was below 1 K. Therefore we performed all subsequent experiments at spinning speeds smaller than 2.5 kHz, in order to observe only heating caused by rf fields.

For the characterization of the temperature increase as function of the applied B_1 field, we used an rf pulse sequences for heating experiments proposed by several authors [12,13,16] as illustrated in Fig. 9a. A typical pulse sequence consisted of a "heating pulse" generated by variable power levels on the proton channel followed by a delay and a π/2-pulse on the observation channel. In our

Table 3
Comparison of the B_1 efficiency for the solenoid and the LLC resonator

Resonator	NMR data				
	η_P Adamantane [kHz/$\sqrt{W}$]	η_P Glycine [kHz/$\sqrt{W}$]	η_P CaM [kHz/$\sqrt{W}$]	ΔT at rf of 100 kHz Ethyl. glyc. [K]	$I_{810°}/I_{90°}$ 5.5 mm sample adamantane/glycine [%]
700 MHz					
Solenoid	13.6	13.3	10.4	51.7	55
LLC	10.0	9.7	9.4	3.7	82
176 MHz					
Solenoid	5.1	4.9	—	—	70
LLC	4.2	4.0	—	—	82
71 MHz					
Solenoid	—	2.6	—	—	59
LLC	—	2.1	—	—	91

The B_1 efficiency was measured with samples of adamantane, glycine and a full MAS rotor (42 μl) of calmodulin. The temperature increase ΔT after the irradiation of an ^{1}H pulse of 50 ms at $f_1 = 100$ kHz amplitude was measured using ethylene glycol as chemical shift thermometer. To obtain a measure for the B_1 homogeneity, we determined the ratio I_{810}/I_{90} of the NMR signal intensity after a 810° pulse related to the intensity after a 90° pulse.

case we applied a duration of 50 ms for the heating pulse, 100 ms for the delay, and 5 dummy scans to allow thermal equilibrium.

For the probe equipped with the solenoid at $f_1 = 60$ kHz proton field amplitude, the sample temperature increased by a maximum of 31 K with a temperature gradient of ~13 K across the sample. For the LLC under the same experimental conditions, the maximum temperature difference was below 1 K (Fig. 10).

A second set of experiments was run to measure the evolution of the temperature throughout the sample during and after a long decoupling pulse of $\nu_1 = 100$ kHz proton field amplitude (Fig. 11). The pulse sequence is illustrated in Fig. 9b and consists of a $(\pi/2)_x$ pulse followed by a heating/spinlock pulse of length $p15$ and a $(\pi/2)_{-x}$ pulse. After a delay $d5$ another $\pi/2$ pulse is applied before aquisition starts.

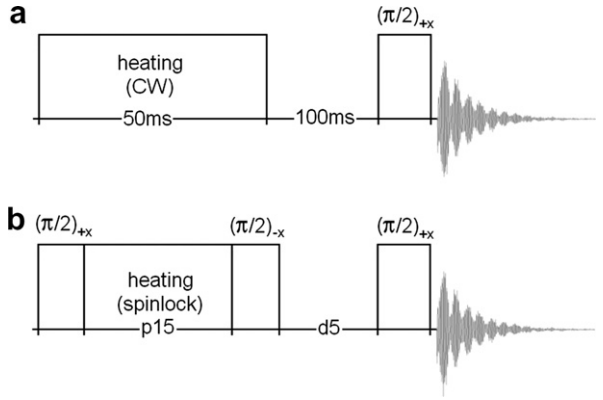

Fig. 9. ^{1}H Pulse sequences used for the heating experiments. (a) heating pulse of 50 ms to mimic a long decoupling pulse followed by a 100 ms delay and a $\pi/2$ detection pulse. (b) Pulse sequence to track the heat evolution: after an initial $(\pi/2)_{+x}$ pulse, a heating/spin lock pulse of variable duration $p15$ is applied and terminated by a $(\pi/2)_{-x}$ pulse to flip back the magnetization. After the variable delay $d5$ the spectrum is acquired. Varying $p15$ and $d5$ and using an NMR chemical shift thermometer, the temperature evolution during and after a pulse can be observed.

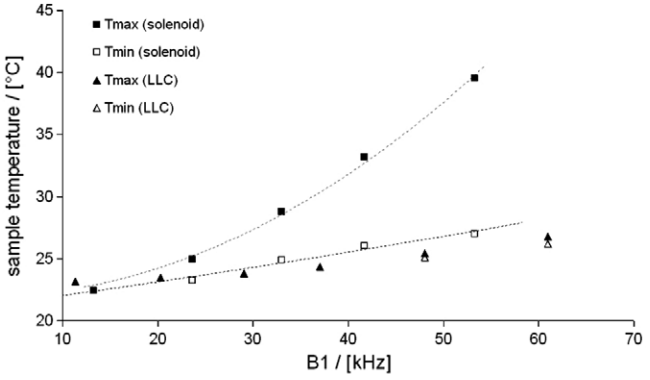

Fig. 10. Temperature increase in a 42 μl ethylene glycol sample centered in the coil as function of the B_1 field amplitude after a 50 ms heating pulse on the ^{1}H channel. The temperature was derived from the temperature dependent chemical shift of the –OH protons. The solid and light symbols correspond to the maximum and minimum temperature across the sample volume 100 ms after the heating pulse was switched off. For the solenoid exciting the sample with a B_1 field amplitude of $f_1 = 60$ kHz the peak temperature in the sample is increased by 31 K with a temperature gradient of 13 K. Using the LLC under the same experimental conditions exhibits a maximum temperature gradient <1 K. Data were taken under MAS at 2.5 kHz.

During the first 6 experiments, the spin lock/heating pulse was set to $p15 = 0$, 10, 20, 30, 40, 50 ms keeping the delay fixed at $d5 = 0$ ms. To track the heat evolution after the pulse, $d5$ was increased and the heating pulse $p15$ kept unchanged at 50 ms. The heat deposition in the sample is illustrated by the temperature shift of the –OH peaks in ethylene glycol with a temperature dependence of -9.75×10^{-3} ppm/K in the temperature range from 300 to 380 K (Fig. 11a and b). While the broadening of the hydroxyl peak measured with the solenoidal coil spans 0.44 ppm corresponding to a temperature gradient of 50 K over the length of the sample directly after the heating pulse (Fig. 11a), this broadening amounts to be less than 0.1 ppm for the LLC (Fig. 11b). The time constant of the temperature decay after the heating pulse is on the order of several seconds.

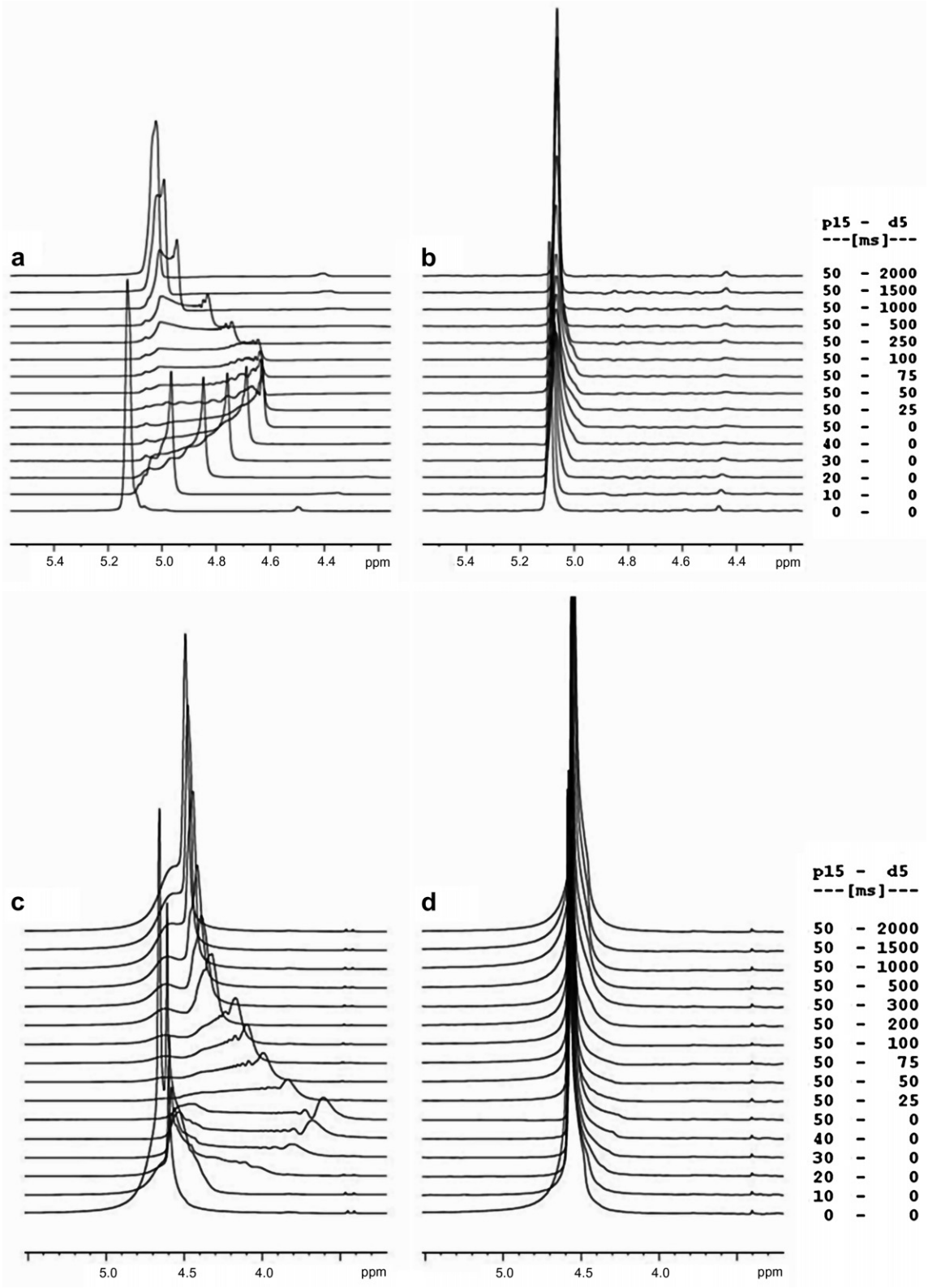

Fig. 11. Evolution of the temperature dependent shift of the –OH peak of ethylene glycol during and after a 50 ms decoupling pulse at $f_1 = 100$ kHz B_1 field amplitude (a) for a solenoid and (b) for the LLC. During the experiment the VT gas temperature was set to 290 K. The maximum temperature gradient of ~50 K is observed after the heating pulse. (c) and (d) show the same experiment as in (a and b) with VT set to 280 K and observing the water peak of the CaM sample. The temperature dependence of the water peak was determined to be 114–121 K/ppm in the range from 275 to 295 K. It indicates a massive temperature increase during the $f_1 = 100$ kHz heating pulse in the solenoid. For the LLC, (b) and (d), no such significant temperature gradient was observed.

We repeated these experiments with a microcrystalline sample of the protein calmodulin (CaM) crystallized from a starting protein solution of 18 mg/ml CaM, 100 mM NaCl, 50 mM Tris–HCl, 1 mM $CaCl_2$, at pH 8.0, precipitated with equal volume of 40% MPD, 200 mM di-ammonium phosphate (sample provided by courtesy of C. Luchinat and I. Bertini, CERM, Florence, and prepared by G. Pintacuda, ENS Lyon). This procedure led to a sample which was not suitable for further study, because it could not be matched and tuned on a conventional triple resonance CPMAS probe without modifying the circuit (see Section 4.2).

The broadening of the water peak of the CaM sample due to the temperature distribution across the sample at $\nu_1 = 100$ kHz proton field is illustrated in Fig. 11c and d. The thermal broadening of the water peak of CaM is equal to 1.1 ppm for the solenoid (Fig. 11c) as compared with ~0.2 ppm for the LLC (Fig. 11d).

During the experiment we cooled the sample by a constant air flow from an Bruker BCU-X cooling unit through the VT channel with a sample temperature set to 280 K. Prior to the experiment we determined the temperature dependence of the water peak as $-8.27\ldots-8.76\times 10^{-3}$ ppm/K in the range from 275 to 295 K.

For the solenoidal coil, a 24% decrease of the B_1 efficiency at the proton channel was observed, due to the higher sample conductivity (10.4 kHz/$\sqrt{\text{W}}$ as compared with 13.6 kHz/$\sqrt{\text{W}}$ for adamantane). This is in contrast to the LLC where the B_1 efficiency was almost unaffected within the accuracy of the measurement (Fig. 8).

4.4. NMR sensitivity under high-power decoupling

In order to illustrate the robustness of the LLC geometry we performed ^{1}H/^{13}C cross-polarization experiments on glycine and our lossy calmodulin sample with decoupling field amplitudes of 110 and 100 kHz. The ^{13}C sensitivity was measured with a full 3.2 mm rotor (sample volume 42 μl) of glycine at 7 kHz MAS frequency and after 4 scans with a duty cycle of 5 s. During the contact time the ^{13}C spin system was polarized with $f_1 = 50$ kHz applying at the same time a 50–100% ramped pulse at 68 kHz on the ^{1}H channel. During the 16 ms acquisition time spinal-64 decoupling [46] with an rf amplitude of $f_1 = 110$ kHz was applied (Fig. 12).

Under these experimental conditions the mean signal-to-noise ratio (S/N) of C_α carbon after four scans was equal to (107 ± 5):1 and (114 ± 5):1 for the LLC and the solenoid, respectively, based on 10 consecutive experiments and measured with a 10 ppm noise range over the entire spectrum. This corresponds to a drop in ^{13}C sensitivity of 10–20% for the LLC with respect to the sensitivity achieved with the solenoid. Note that this observation correlates well with the predicted reduction of the carbon B_1 efficiency η_P for the glycine sample ($\eta_{P,LLC} = 4.0$ kHz/$\sqrt{\text{W}}$ and $\eta_{P,sol} = 4.9$ kHz/$\sqrt{\text{W}}$ corresponding to a decrease of 18%). The linewidth at half maximum of the C_α-peak was found to be 57.5 ± 0.3 Hz.

However, the efficiency of the polarization transfer depends on an efficient matching of the B_1 field amplitudes across the sample during contact. Although the homogeneity of the LLC is superior to the solenoid, we did not observe a substantial improvement. We attribute this to the fact, that the relative B_1 homogeneity, e.g., the B_1 field profiles at proton and carbon frequencies, are well matched for the solenoid (despite their lower overall homogeneity).

Additionally, we performed CP experiments with similar CP parameters at an rf amplitude of $\nu_1 = 100$ kHz during spinal-64 decoupling, with the highly lossy calmodulin sample (Fig. 13a and b). After 512 scans the intensity of

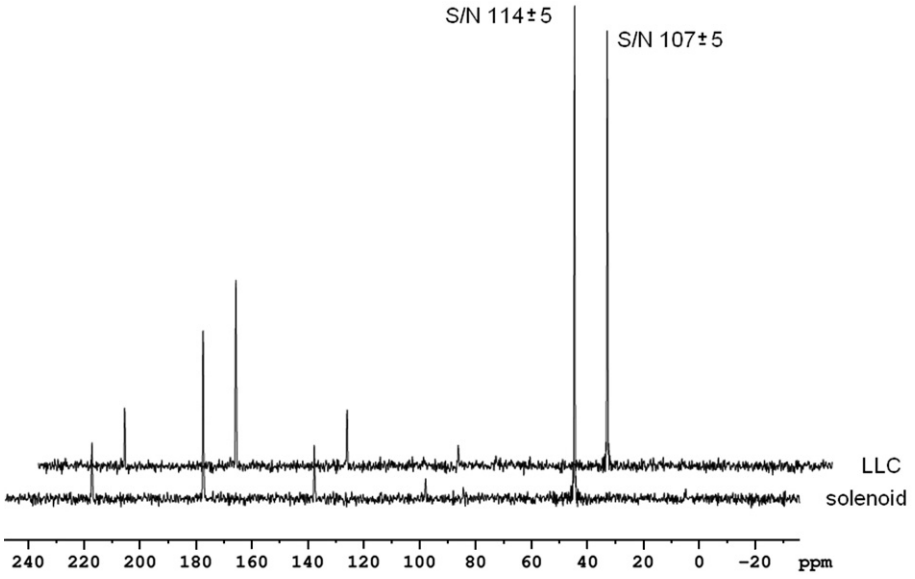

Fig. 12. Stacked ^{1}H/^{13}C CP spectra of glycine acquired with the solenoidal coil and the LLC after 4 scans at an MAS spinning rate of 7 kHz. In the proton channel, a 1 ms 50–100% ramp was used during CP contact, where 100% corresponds to an rf amplitude of $f_1 = 68$ kHz. A rectangular ^{13}C contact pulse with amplitude 50 kHz was applied. During acquisition ^{1}H was decoupled using the spinal-64 sequence with rf amplitude of 110 kHz. The linewidth of the C_α peak amounted to be <57 Hz in both cases.

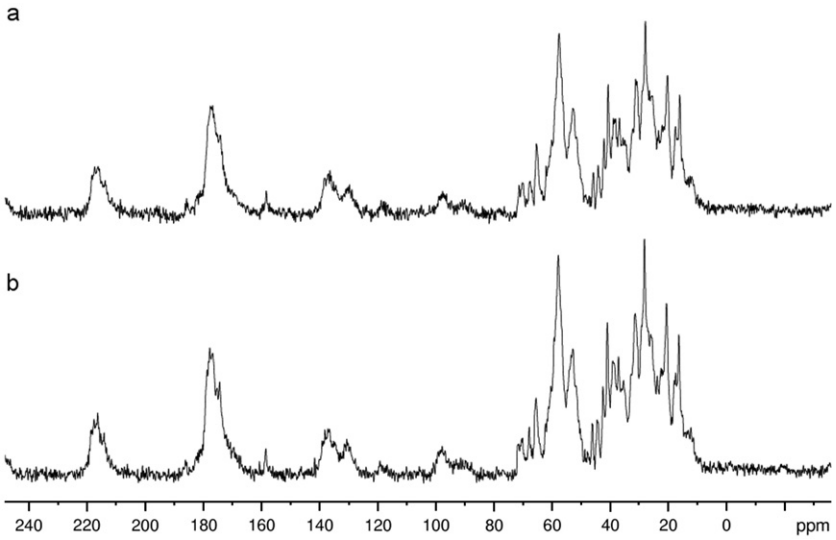

Fig. 13. ^{1}H–^{13}C CP spectra of calmodulin (a) performed with the LLC and (b) with the solenoid after 512 scans at 7 kHz MAS rotation frequency. A ramp pulse of 1 ms duration with 50–100% variable amplitude was used during contact where 100% correspond to 68 kHz ^{1}H rf field amplitude. The ^{13}C contact pulse had rectangular shape with 50 kHz amplitude. During acquisition the ^{1}H was decoupled using spinal-64 at 100 kHz.

the spectrum acquired with the LLC is 80% of the intensity measured with the classical solenoid.

5. Conclusion

An efficient NMR coil geometry for solid-state MAS—the LLC resonator—has been presented that provides a high B_1 homogeneity while reducing efficiently the rf electric fields E_1 in the sample volume. The basic principle of he LLC has been derived by straightforward application of boundary conditions for the electromagnetic field and further refined by numerical simulation. From the explicit numerical solution of the electromagnetic field for a model system and by comparing a classical solenoidal coil with an LLC, filling factors and Q values were calculated and compared with experimental data.

The NMR features of the LLC were evaluated by comparing it with a solenoidal coil with respect to B_1 efficiency, B_1 homogeneity, sample heating and NMR sensitivity. For lossless samples, the measurement of the B_1 efficiency confirmed the solenoidal coil as the more efficient geometry to be used in NMR. However, the LLC proved its stability for standard high power decoupling experiments while the S/N was reduced by only 10–20% for glycine as compared to the same measurement with the solenoid. The LLC coil has high rf magnetic field homogeneity, which may be useful for high-resolution ^{1}H NMR application.

However, when the sample is lossy, usually the case for solid protein NMR samples, the LLC coil comes into its own. In these cases shown here we observed virtually no change in tuning properties for the LLC coil with a highly lossy protein sample. Similarly, we see virtually no sample heating effects in this coil, allowing high power solid-state NMR experiments to be used without endangering the sample. For such samples, the LLC coil is clearly superior to a solenoidal coil.

Acknowledgments

We express our deep gratitude to Gerhard Althoff (Bruker Biospin), Jim Davis (University of Guelph), and Baudouin Dillmann (formerly Bruker Biospin) for fruitful discussions, and to Ivano Bertini, Claudio Luchinat, Paul Ionescu (CERM Florence) and Guido Pintacuda (ENS Lyon) for providing the calmodulin sample and for help obtaining the spectra of Fig. 13.

References

[1] D.G. Gadian, F.N.H. Robinson, Radiofrequency losses in NMR experiments on electrically conducting samples, J. Magn. Reson. 34 (1979) 449–455.
[2] S.V. Dvinskikh, V. Castro, D. Sandström, Heating caused by radiofrequency irradiation and sample rotation in ^{13}C magic angle spinning NMR studies of lipid membranes, Magn. Reson. Chem. 42 (2004) 875–881.
[3] C. Li, Y. Mo, J. Hu, E. Chekmenev, Ch. Tian, F.P. Gao, R. Fu, P. Gorkov, W. Brey, T.A. Cross, Analysis of rf heating and sample stability in aligned static solid-state NMR spectroscopy, J. Magn. Reson. 180 (2006) 51–57.
[4] P.V. Yushmanov, I. Furó, A temperature-jump design for conventional NMR probes, J. Magn. Reson. 181 (2006) 148–153.
[5] G.G. Maresch, R.D. Kendrick, C.S. Yannoni, High-temperature NMR using inductive heating, Rev. Sci. Instrum. 61 (1990) 77–80.
[6] T. Horiuchi, M. Takahashia, J. Kikuchia, S. Yokoyamaa, H. Maeda, Effect of dielectric properties of solvents on the quality factor for a beyond 900 MHz cryogenic probe model, J. Magn. Reson. 174 (2005) 34–42.
[7] A.E. Kelly, H.D. Ou, R. Withers, V. Dötsch, Low-conductivity buffers for high-sensitivity NMR measurements, J. Am. Chem. Soc. 124 (40) (2002) 12013–12019.

[8] S. Crozier, I.M. Brereton, F.O. Zelaya, W.U. Roffmann, D.M. Doddrell, Sample-induced rf perturbations in high-field, high-resolution NMR spectroscopy, J. Magn. Reson. 126 (1997) 39–47.
[9] R. Wimmer, G. Wider, Real-time imaging of the spacial distribution of rf-heating in NMR samples during broadband decoupling, J. Magn. Reson. 187 (2007) 184–192.
[10] M. Simeonova, J. Gimsa, The influence of the molecular structure of lipid membranes on the electric field distribution and energy absorption, Bioelectromagnetics 27 (2006) 652–666.
[11] F. Engelke, Electromagnetic wave compression and radio frequency homogeneity in NMR solenoidal coils: computational approach, Concepts Magn. Reson. B 15 (2002) 129–155.
[12] J.A. Stringer, C.E. Bronnimann, G. Mullen, D.H. Zhou, S.A. Stellfox, Y. Li, E.H. Williams, C.M. Rienstra, Reduction of rf-induced sample heating with a scroll coil resonator structure for solid-state NMR probes, J. Magn. Reson. 173 (2005) 40–48.
[13] B. Dillmann, K. Elbayed, H. Zeiger, M.-C. Weingertner, M. Piotto, F. Engelke, A novel low-E field coil to minimize heating of biological samples in solid-state multinuclear NMR experiments, J. Magn. Reson. 187 (2007) 10–18.
[14] L.A. Crum, K.W. Zilm, Resonator design for decreasing sample heating in solid state NMR experiments, in: 47th ENC, Daytona Beach, 2007.
[15] D.W. Alderman, D.M. Grant, An efficient decoupler coil design which reduces heating in conductive samples in superconducting spectrometers, J. Magn. Reson. 36 (1979) 447–451.
[16] F.D. Doty, J. Kulkarni, C. Turner, G. Entzminger, A. Bielecki, Using a cross-coil to reduce rf heating by an order of magnitude in triple-resonance multinuclear MAS at high fields, J. Magn. Reson. 182 (2006) 239–253.
[17] P.L. Gor'kov, E. Chekmenev, R. Fu, J. Hu, T.A. Cross, M. Cotton, W.W. Brey, A large volume flat coil probe for oriented membrane proteins, J. Magn. Reson. 181 (2006) 9–20.
[18] P.L. Gor'kov, E. Chekmenev, C. Li, M. Cotten, J.J. Buffy, N.J. Traaseth, G. Veglia, W.W. Brey, Using low-E resonators to reduce rf heating in biological samples for static solid-state NMR up to 900 MHZ, J. Magn. Reson. 185 (2007) 77–93.
[19] P.L. Gor'kov, R. Witter, E. Chekmenev, F. Nozirov, R. Fu, W. Brey, Low-E probe for 19F-^{1}H NMR of dilute biological solids, J. Magn. Reson. 190 (2007) 17–24.
[20] D.I. Hoult, R.E. Richards, The signal-to-noise ratio of the nuclear magnetic resonance experiment, J. Magn. Reson. 24 (1976) 71–85.
[21] K. Simonyi, Theoretische Elektrotechnik, eighth ed., Deutscher Verlag der Wissenschaften, 1980.
[22] E.K. Insko, M.A. Elliott, J.C. Schotland, J.S. Leigh, Generalized reciprocity, J. Magn. Reson. 131 (1998) 111–117.
[23] J.J. van der Klink, The NMR reciprocity theorem for arbitrary probe geometry, J. Magn. Reson. 148 (2001) 147–154.
[24] F.D. Doty, Probe design and construction, in: D.M. Grant, R.K. Harris (Eds.), Encyclopedia of NMR, Wiley, 1996.
[25] W. Froncisz, J.S. Hyde, The loop-gap resonator: a new microwave lumped element circuit ESR sample structure, J. Magn. Reson. 47 (1982) 515–521.
[26] M. Mehdizadeh, T.K. Ishii, J.S. Hyde, W. Froncisz, Loop-gap resonator: a lumped mode microwave resonant structure, Trans. Microwave Theor. Techn. MTT-31 (1983) 1059–1063.
[27] R.F. Harrington, Time-Harmonic Electromagnetic Fields, IEEE Press Classic Reissue, Wiley, 2001.
[28] D.J. Cory, J.T. Lewandowski, W.E. Maas, NMR probe for cross-polarization measurements. US Patent 5539315, 1996.
[29] D. Sakellariou, G. Le Goff, J.-F. Jacquinot, High-resolution, high-sensitivity NMR of nanolitre anisotropic samples by coil spinning, Nature 447 (2007) 646–647.
[30] J.W. Carlson, Currents and fields of thin conductors in rf saddle coils, Magn. Reson. Med. 3 (5) (1986) 778–790.
[31] T. Weiland, A discretization method for the solution of Maxwell equations for six-component fields, AEÜ 31 (1977) 116–120.
[32] Microwave Studio, Computer Simulation Technologies—CST, Darmstadt, Germany, <http://www.cst.com/>.
[33] W. Sichak, Coaxial line with helical inner conductor, Proc. IRE 42 (1952) 1315–1319.
[34] L. Stark, Lower modes of a concentric line having a helical inner conductor, J. Appl. Phys. 25 (9) (1954) 1155–1162.
[35] S. Sensiper, Electromagnetic wave propagation on helical structures, Proc. IRE 43 (1955) 149–161.
[36] F.D. Doty, G. Entzminger, Y.A. Yang, Magnetism in high-resolution NMR probe design. I: general methods, Concept. Magn. Reson. 10 (1998) 133–156.
[37] F.O. Zelaya, S. Crozier, S. Dodd, R. McKenna, D.M. Doddrell, Measurement and compensation of field inhomogeneities caused by differences in magnetic susceptibility, J. Magn. Reson A 115 (1995) 131–135.
[38] V.R. Cross, R.K. Hester, J.S. Waugh, Single coil probe with transmission-line tuning for nuclear magnetic double-resonance, Rev. Sci. Instrum. 47 (1976) 1486–1488.
[39] L. Maier, J. Slater, Field strength measurement in resonant cavities, J. Appl. Phys. 23 (1952) 68–77.
[40] A.L. Van Geet, Calibration of the methanol and glycol nuclear magnetic resonance thermometers with a static thermistor probe, Anal. Chem. 40 (14) (1968) 2227–2229.
[41] M.L. Kaplan, F.A. Bovey, H.N. Cheng, Simplified method of calibrating thermometric nuclear magnetic resonance standards, Anal. Chem. 47 (1975) 1703–1705.
[42] C. Amman, P. Meier, A.E. Merbach, A simple multinuclear NMR thermometer, J. Magn. Reson. 46 (1982) 319–321.
[43] C.S. Zuo, K.R. Metz, Y. Sun, A.D. Sherry, NMR temperature measurements using a paramagnetic lanthanide complex, J. Magn. Reson. 133 (1998) 53–60.
[44] W. Sikorski, A. Sanders, H. Reich, Tris(trimethylsilyl)methane as an internal ^{13}C NMR chemical shift thermometer, Magn. Reson. Chem. 36 (1998) 118–124.
[45] R.C. Weast, M.J. Astle, W.H. Beyer (Eds.), CRC Handbook of Chemistry and Physics, sixty-fifth ed., CRC Press, Boca Raton, Florida, 1984, p. E-51.
[46] B.M. Fung, A.K. Khitrin, K. Ermolaev, An improved broadband decoupling sequence for liquid crystals and solids, J. Magn. Reson. 142 (1) (2000) 97–101.